nanomaterials

MDPI

Article

Optimized Thermoelectric Properties of Sulfide Compound Bi_2SeS_2 by Iodine Doping

Chongbin Liang, Bushra Jabar, Chen Liu, Yuexing Chen, Zhuanghao Zheng, Ping Fan and Fu Li *

Shenzhen Key Laboratory of Advanced Thin Films and Applications, College of Physics and Optoelectronic Engineering, Shenzhen University, Shenzhen 518060, China; 2060451017@email.szu.edu.cn (C.L.); bushrajabbar_786@outlook.com (B.J.); 2070456054@email.szu.edu.cn (C.L.); chenyx@szu.edu.cn (Y.C.); zhengzh@szu.edu.cn (Z.Z.); fanping@szu.edu.cn (P.F.)
* Correspondence: lifu@szu.edu.cn

Abstract: The Te-free compound Bi_2SeS_2 is considered as a potential thermoelectric material with less environmentally hazardous composition. Herein, the effect of iodine (I) substitution on its thermoelectric transport properties was studied. The electrical conductivity was enhanced due to the increased carrier concentration caused by the carrier provided defect I_{se}. Thus, an enhanced power factor over 690 $\mu Wm^{-1}K^{-2}$ was obtained at 300 K by combining a moderate Seebeck coefficient above 150 $\mu V/K$ due to its large effective mass, which indicated iodine was an effective n-type dopant for Bi_2SeS_2. Furthermore, a large drop in the lattice thermal conductivity was observed due to the enhanced phonon scattering caused by nanoprecipitates, which resulted in a low total thermal conductivity (<0.95 $Wm^{-1}K^{-1}$) for all doped samples. Consequently, a maximum ZT value of 0.56 was achieved at 773 K for a $Bi_2Se_{1-x}I_xS_2$ (x = 1.1%) sample, a nearly threefold improvement compared to the undoped sample.

Keywords: thermoelectric material; Bi_2SeS_2; doping; thermoelectric property

Citation: Liang, C.; Jabar, B.; Liu, C.; Chen, Y.; Zheng, Z.; Fan, P.; Li, F. Optimized Thermoelectric Properties of Sulfide Compound Bi_2SeS_2 by Iodine Doping. *Nanomaterials* **2022**, *12*, 2434. https://doi.org/10.3390/nano12142434

Academic Editor: Alexander I. Gusev

Received: 24 May 2022
Accepted: 13 July 2022
Published: 15 July 2022

1. Introduction

Thermoelectric (TE) materials directly convert electrical and thermal energy without emitting harmful substances and are considered environmentally friendly materials with huge development potential and broadly applicability [1–4]. Generally, the energy conversion efficiencies of TE materials are evaluated by ZT ($ZT = \sigma S^2 T/\kappa$), where σ, S, κ, and T are the electrical conductivity, Seebeck coefficient, thermal conductivity, and the absolute temperature, respectively [5–7]. Therefore, an outstanding TE material should have a high ZT with high electrical conductivity, large Seebeck coefficient, and low thermal conductivity. The optimization of these intuitive interdependent parameters poses a significant challenge. However, the design of rational experimental strategies has continuously rewritten the record of ZT over the past twenty years [8–13].

As two important conventional TE materials, Bi_2Te_3 and PbTe are the best and most stable materials used near room temperature and mid-temperature [14,15]; however, large-scale commercial applications in the future are limited due to the extensive use of toxic Pb and Te [16]. Thus, developing Te-free and Pb-free candidates with high TE performance represents a significant and important challenge [17,18]. Recently, environmentally friendly sulfide compounds have received widespread attention. Bi_2S_3 is a typical example of the sulfide counterpart of Bi_2Te_3, with a similar crystal structure [19,20]. Despite its poor electrical conductivity and high thermal conductivity that results in a dismally low ZT (0.055), TE properties have been optimized using several effective strategies, which include elemental doping, texturing, and microstructure design [21–26]. However, most reported ZT values are < 0.6, relatively low compared to traditional materials [21–26]. Poor TE properties for the sulfide compounds stem primarily from low electrical conductivity and

high lattice thermal conductivity due to the light atomic weights and either too high or too low carrier concentrations.

Recent reports revealed that the ternary sulfide compound Bi_2SeS_2 has TE potential with a high *ZT* (>1.0) [27,28]. Its crystalline structure was similar to Bi_2S_3. But the Bi_2SeS_2 band gap of ~1.0 eV was narrower than Bi_2S_3 (~1.35 eV), which caused reasonably satisfactory electrical conductivity. Combined with low thermal conductivity (<0.8 W $m^{-1}K^{-1}$), a *ZT* value of 0.25 was obtained for the pure sample [29]. By tuning the electrical conductivity via Cu doping and suppressing the lattice thermal conductivity by forming nanoprecipitates, the *ZT* value increased to 0.7 at 723 K, and to 1.0 at 773 K [27,30]. Recently, Br served as an effective carrier donor and induced a partial Bi_2SeS_2 phase change from *Pnma* to *Pnnm*, which formed a quasi homo-composition and a hetero-structure (*ho*C-*he*S) nanocomposite [28]. This caused a significant lattice thermal conductivity decrease and enhanced power factor, which resulted in a large *ZT* value improvement.

Halogens are well-known n-type dopants for the Bi_2X_3 family (X = Te, Se, and S), with defects in Cl_x, Br_x, or I_x providing free electrons to increase carrier concentrations [31,32]. Aside from Br doping, the effect of single Cl or I doping on TE transport properties of Bi_2SeS_2 has not been reported. Whether Cl or I would induce the phase transition of Bi_2SeS_2 merits consideration. Hence, this motivated us to conduct this study. Herein, iodine (I) was chosen as a dopant in the Bi_2SeS_2 system. Although no phase transition was found after iodine doping, an enhanced power factor due to the increased carrier density, together with a reduced lattice thermal conductivity due to the enhanced phonon scattering, was obtained. A maximal *ZT* of 0.56 at 773 K was achieved for $Bi_2Se_{1-x}I_xS_2$ with x = 1.1%, three times higher than the undoped sample, which indicated iodine was an effective n-type dopant for Bi_2SeS_2.

2. Experimental

A series of $Bi_2Se_{1-x}I_xS_2$ (x = 0, 0.1%, 0.3%, 0.5%, 0.7%, 0.9%, 1.1%, and 1.3%) ingots were synthesized by a combination of solid-state reaction and spark plasma sintering (SPS) using high-purity powders of Bi (99.99%), Se (99.99%), S (99.95%) and BiI_3 (99.99%). Stoichiometric powder mixtures were roughly mixed and placed into glass ampoules according to their compositions. The ampoules were sealed under vacuum (<10^{-3} Pa) and heated at 1173 K for 12 h with subsequent annealing at 773 K for 48 h. Ingots were obtained upon cooling to 300 K and pulverized into micron-sized powders by hand grinding. The powder was placed into a mold and sintered in as SPS furnace at 773 K for 5 min with an axial pressure of 50 MPa to form column-shaped bulk sample. Two pieces were obtained from one bulk sample. One piece was used to measure the electrical conductivity and Seebeck coefficient along the direction perpendicular to the SPS pressing direction; the other piece was used to test its thermal conductivity in the same direction.

Crystal structures were determined by X-ray diffraction (XRD, Ultima IV, Riguku, Japan) using Cu Kα radiation and a scanning rate of 5°/min. Rietveld refinement was performed using the Generalized Structural Analysis System (GSAS-II) program. The micromorphologies of the fractured surfaces and backscattered electron imaging (BES) on the polished surfaces were detected via field scanning electron microscopy (FSEM, Supra 55 Sapphire, Zeiss, Germany). The energy dispersive spectroscopy (EDS) equipment attached to the FSEM analyzed the elemental compositions and distributions. The electrical resistivity and the Seebeck coefficient were measured from room temperature to 773 K using an electric resistance/Seebeck coefficient measuring system (ZEM-3, Ulvac-Riko, Japan). The Hall coefficients (R_H) at room temperature were tested by a Van der Pauw technique. Based on the expression $\mu = \sigma R_H$ and $n = 1/(eR_H)$, where σ is the electrical conductivity, the carrier mobility (μ) and the carrier concentration (n) were calculated. The thermal diffusivity (D) was determined using laser flash diffusivity (Netzsch LFA467, Germany), which was then used to calculate the total thermal conductivity (κ) using $\kappa = DC_p\rho$, where ρ is the bulk density of the sample, and C_p is the heat capacity. C_p values were tested using two differential scanning calorimeters (DSC); a DSC200-F3 yielded C_p values from

298–523 K; a DSC404-C gave C_p values from 523–773 K. Densities were determined by the Archimedes method.

3. Results and Discussion

The XRD patterns for pristine and doped $Bi_2Se_{1-x}I_xS_2$ (x = 0–1.3%) samples are presented in Figure 1a. The main peaks agree with the standard XRD peaks of Bi_2SeS_2 polycrystalline, simulated from the atomic site occupation and lattice parameters a = 11.5044 Å, b = 4.0254 Å, and c = 11.2959 Å, as reported previously [19]. Reitveld refinement studied the doping-induced structural changes in the Bi_2SeS_2 system further (representative result is shown in Figure 1b). The XRD peaks of all samples match well with an orthorhombic *Pnma* phase. No phase transition can be found as the reported Br doped samples [28]. Figure 1c shows the I dopant-induced lattice parameter evolution, which was derived from the Reitveld refinement. According to the calculated formation energy [28], I preferentially occupies the Se site when doping in Bi_2SeS_2. The ionic radius of I^- (2.2 Å) exceeds Se^{2-} (1.98 Å), which should enlarge the lattice parameters. However, no obvious changes were observed for the three axes (Figure 1c), although slight increase in the *a*- and *c*-axes appears at high doping levels. One possible reason might stem from the low doping levels of I, which cannot cause these changes. Another reason might be ascribed to the volatilization of S, which may offset lattice parameters increases caused by I doping. In addition, a weak impurity peak appeared at ~29.21° in all samples, which corresponded to the BiSe (PDF#42-1045) phase as BiSe has a characteristic peak around this position. This impurity was commonly observed in previous reports for Bi_2SeS_2 systems and is thought to spontaneously form due to thermodynamic stability similar to Bi_2SeS_2 [29].

SEM pictures for the freshly fractured surface perpendicular to the press direction at different x doping levels are shown in Figure 2a–f. All samples show very dense microstructures, which resulted in a relatively high average density of 7.07 gcm^{-3} and very close to the theoretical value (7.12 gcm^{-3}). Grain sizes in the tens of microns range for the undoped sample dropped to 2–5 μm when doped with I, which indicated that iodine inhibited the diffusion of the elements during sintering and prevented the grain growth. The grains are in a lamellar structure and an apparent orientation arrangement was seen in some areas, which suggested a preferential orientation. The composition and the distribution of Bi, S, Se, and I were detected by EDS on the polished surface. In a few areas, a sulfur deficiency was observed as shown in Figure 2h, and associated with the lighter contrast area indicated as [1] in the BES image of Figure 2g, which confirmed that BiSe precipitates formed in the matrix of $Bi_2Se_{1-x}I_xS_2$ (x = 0–1.3%) as mentioned in the XRD results. Iodine was homogeneously distributed in lower doped samples (x < 1.1%), but some areas of iodine enrichment were observed at elevated dopant levels (1.1% and 1.3%, Figure 2h), which indicated that some I did not enter the lattice and x = 1.1% could represent the iodine doping limit in Bi_2SeS_2. Furthermore, a corresponding enrichment of Bi appeared in very few areas for those two samples indicated as [2] in Figure 2h. This might be due to lower Se levels with increasing x in $Bi_2Se_{1-x}I_xS_2$, and decreased sulfur due to the volatilization, causing excess Bi to precipitate. No Bi or I nanoprecipitate peaks were observed in the XRD patterns, mainly because of their extremely low content.

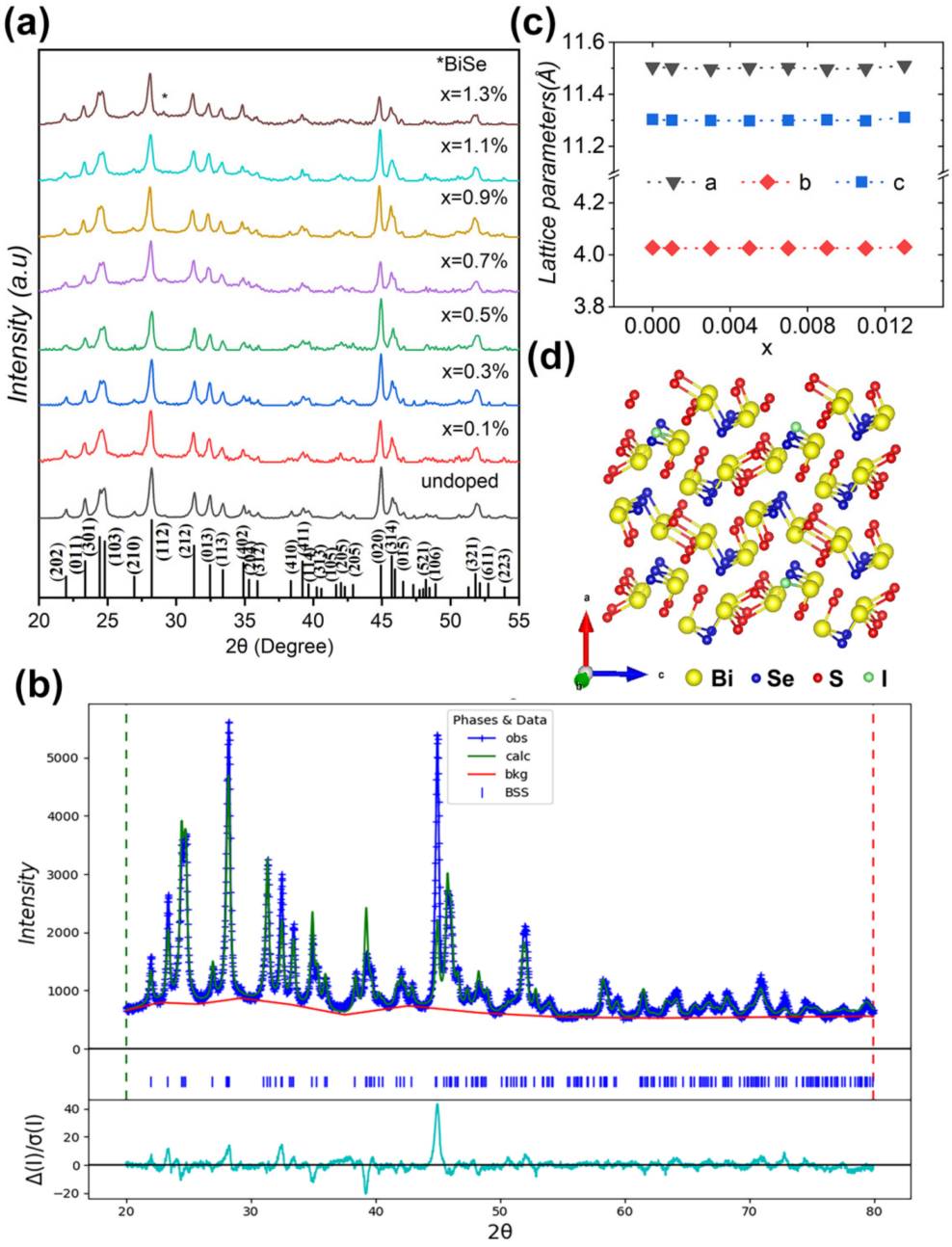

Figure 1. (**a**) XRD patterns for $Bi_2Se_{1-x}I_xS_2$ (x = 0–1.3%). The asterisk represents the impurity peak of BiSe. (**b**) Rietveld refinement analysis from XRD patterns of Bi_2SeS_2, where obs represents observed, calc is calculated, bkg is background, and diff is the residual difference between the curves. (**c**) Variation of lattice parameters with the doped amount x. (**d**) Crystal structure along the *a*-axis for the iodine doped Bi_2SeS_2.

The temperature dependent electrical conductivity (σ), Seebeck coefficient (S), and power factor (PF) for $Bi_2Se_{1-x}I_xS_2$ (x = 0–1.3%) are shown in Figure 3a–c. Figure 3d presents the lattice parameters variation as a function of doping amount at room temperature. The pristine Bi_2SeS_2 sample has a poor σ (20.4 Scm^{-1}) due to its low carrier concentration (n) (Figure 3a) and moderate S (350–400 μVK^{-1}) (Figure 3b), which resulted in a low PF (<2.5 $\mu Wm^{-1}K^{-2}$) as shown in Figure 3c. However, an obviously enhanced σ, up to 100 Scm^{-1}, at 300 K was obtained for $Bi_2Se_{1-x}I_xS_2$ (x = 0.1%), five times higher than the undoped one. The σ roughly increases with increased doping levels (Figure 3d). For instance, increasing the doping levels from 0.3%, 0.5%, and 0.7% improved the σ from 146.3,

202.8 and 253.7 Scm^{-1} (Figure 3d), respectively. This value maximized at 302 Scm^{-1} for the 1.1% sample, although it dropped slightly for $Bi_2Se_{1-x}I_xS_2$ (x = 0.9%). Increasing x to 1.3% lowered the σ at room temperature. But from 300–773 K, the σ of $Bi_2Se_{1-x}I_xS_2$ (x = 1.3%) was better than the others (Figure 3a). As for the temperature-dependent σ, the σ for all doped samples decreased monotonically up to 773 K, which indicated a degenerate semiconductor. However, all data from doped samples exceeded the pristine sample.

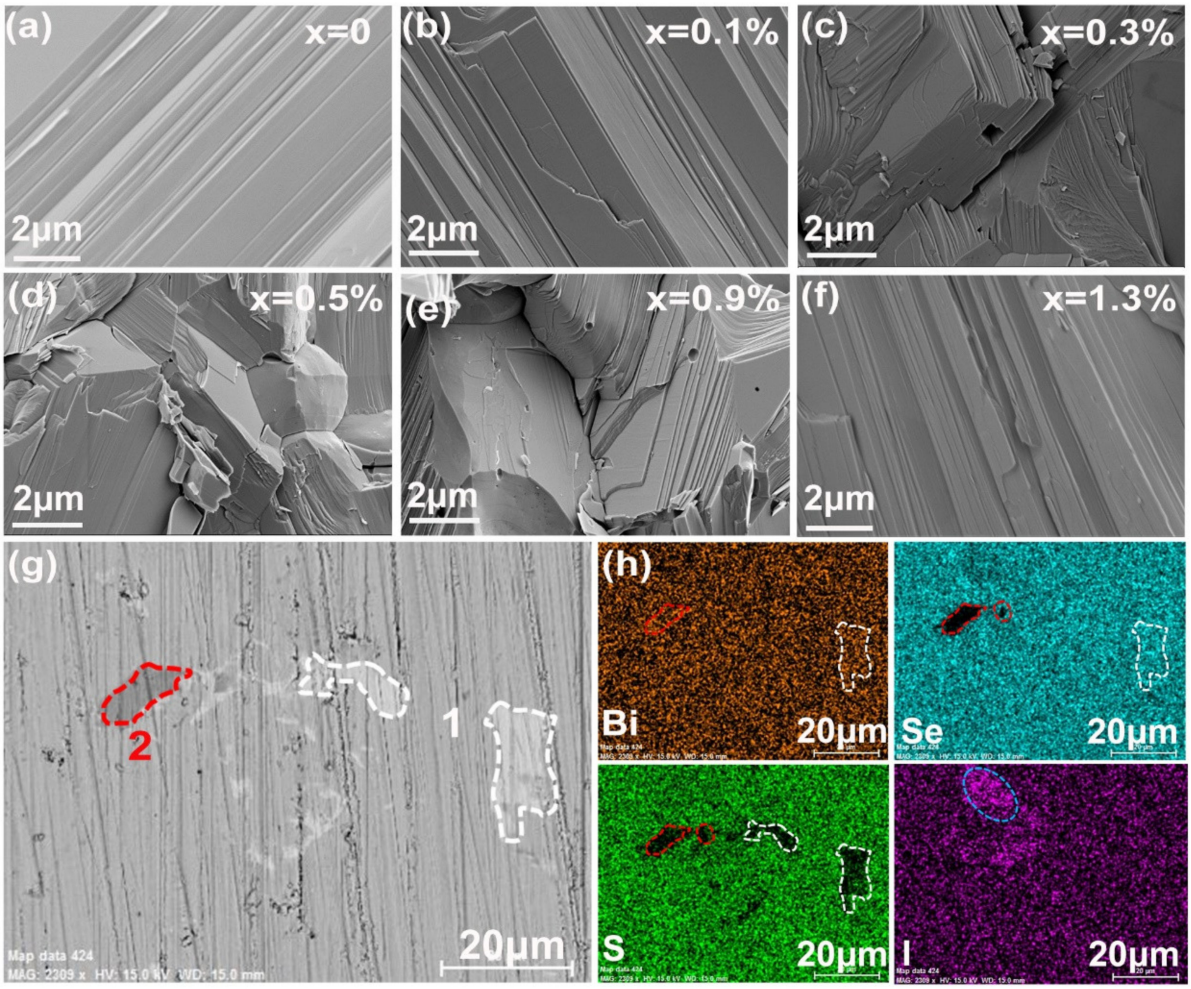

Figure 2. (**a**–**f**) SEM pictures of fresh fracture surfaces for $Bi_2Se_{1-x}I_xS_2$ with x = 0, 0.1%, 0.3%, 0.5%, 0.9%, and 1.3%; (**g**) BES image for $Bi_2Se_{1-x}I_xS_2$ (x = 1.3%). The lighter contrast areas are indicated as 1, while the deep contrast areas are indicated as 2; (**h**) Distribution of the corresponding elements Bi, Se, S and I on the sample surface in (**g**).

The σ was determined by the carrier concentration (n) and carrier mobility (μ) based on the expression of $\sigma = ne\mu$, where e represents the electron charge. Figure 4a shows n and μ as a function of the doping level at room temperature. The pristine sample has a low n of 5.97×10^{18} cm^{-3} caused by S vacancies as follows.

$$Bi_2SeS_2 \rightarrow xS\uparrow + xV_S^{2+} + 2xe^- \quad (1)$$

The upward arrow indicates sulfur volatilization. V_S^{2+} represents an S vacancy. e^- represents an electron. The x in Equation (1) represents the possible amount of S volatilization for the undoped sample. After doping with a small amount of I (x = 0.1%), σ increased to 2.52×10^{19} cm^{-3}. With further increases of the doped content x to 0.3%, 0.5% and 0.7%, the n gradually increased to 3.97×10^{19} cm^{-3}, 5.47×10^{19} cm^{-3} and 9.55×10^{19} cm^{-3}, and maximized at 11.7×10^{19} cm^{-3} when the doped content was 0.9%. This enhancement

should be caused by the carrier provider of I_{se}, according to the following defect chemistry reaction.

$$Bi_2Se_{1-x}S_2I_x \rightarrow xI_{Se}^{+} + xe^{-} \quad (2)$$

The I_{Se}^{+} indicates the replacement of Se by I in the lattice. More electron carriers were supplied if the iodine replaced Se in Bi_2SeS_2, which indicated I was an efficient dopant. This also confirmed that most iodine entered the lattice although some volatilized during sintering. Further increasing the doping levels to x = 1.1% and 1.3% caused the n to decrease to 8.41×10^{19} and 7.65×10^{19} cm^{-3}. As mentioned above, I doping reaches the doping limit at x = 1.1%. In this situation, excessive levels of I can form nanoprecipitates as secondary phases. The interfaces between the secondary phases can significantly filter or block the electron carriers, which lowered n. The μ changes with increasing doping levels as shown in Figure 4a. Firstly, the value of μ slightly increases from 21.1 $cm^2V^{-1}s^{-1}$ for the pristine sample to 22.2 $cm^2V^{-1}s^{-1}$ and 23.5 $cm^2V^{-1}s^{-1}$ when the sample doped with small amounts of x = 0.1% and 0.3%. It then decreases to 22.5, 15.5 and 12.7 $cm^2V^{-1}s^{-1}$ with further increasing of the doped content x to 0.5%, 0.7% and 0.9%. Since n improved after iodine doping, the carrier-carrier scattering might be one of the scattering mechanisms causing the change of μ. In addition, the lattice imperfections introduced by I doping, impurity phases, and their phase boundaries could further scatter the carriers, which also play an important role in the carrier scattering. For samples doped with x = 1.1% and 1.3%, μ increases to 19.2 and 20 $cm^2V^{-1}s^{-1}$ due to reduced carrier scattering, since the iodine doping reaches its limit as mentioned above. Moreover, grain sizes for samples doped with x = 1.1% and 1.3% increased as compared to samples with lower doped levels as shown in Figure 2, which also reduces carrier scattering because of the decreased grain boundary concentration. Combined with the n data, the increase of σ for the doped samples primarily resulted from the increase of n, while the reduced data for the doped sample with x = 0.9% was attributed to the reduced μ. Moreover, the improved σ and n for samples doped with x < 1.1% indicated that electron doping (I) successfully occurred in the Bi_2SeSe_2 system.

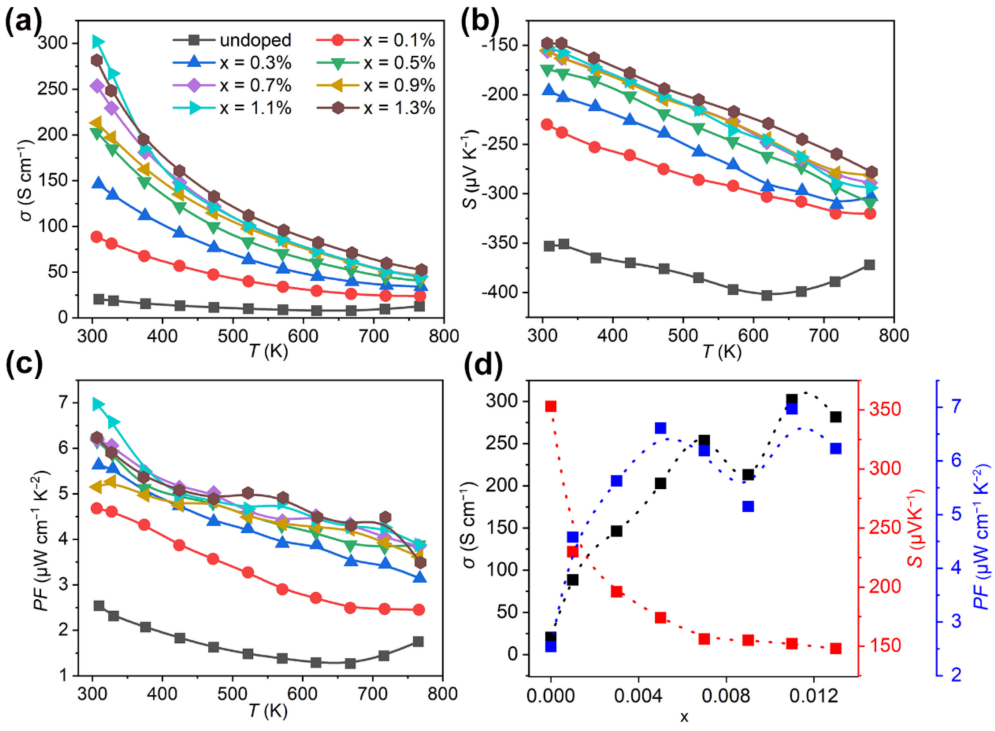

Figure 3. Temperature dependence of (**a**) electrical conductivity (σ), (**b**) Seebeck coefficient (*S*) and (**c**) power factor (*PF*) for $Bi_2Se_{1-x}I_xS_2$ (x = 0–1.3%). (**d**) Change of electrical transport parameters (σ, *S* and *PF*) with doping level at room temperature.

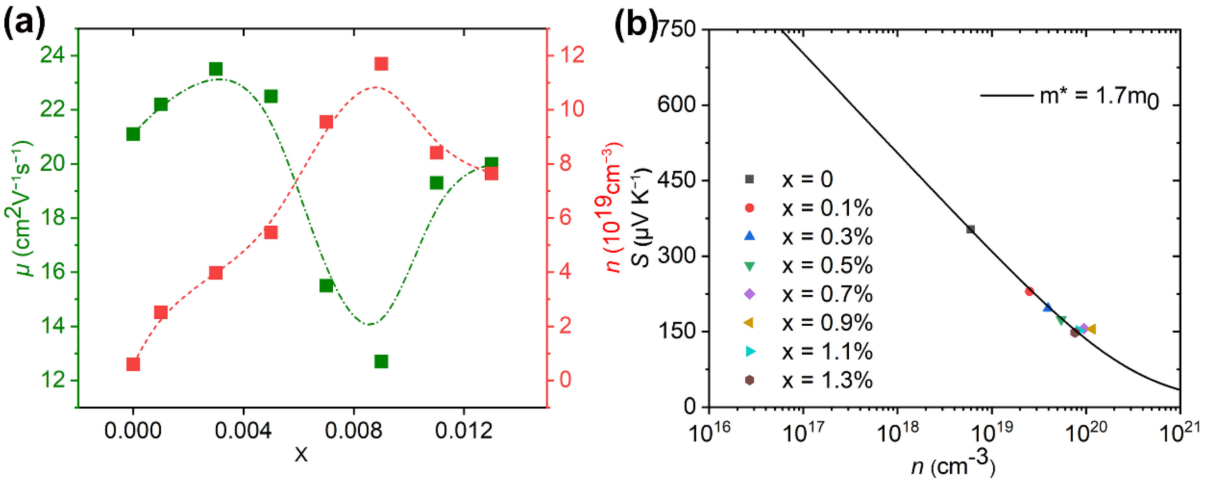

Figure 4. (**a**) Change of carrier concentration (n) and carrier mobility (μ) with doping content x, (**b**) Change of Seebeck coefficient (S) with carrier concentration (n). The line in (**b**) was calculated by the SPB model discussed in detail elsewhere [28,33]. m^* is the electron effective mass at the Fermi level.

Figure 3b shows the Seebeck coefficient (S) for $Bi_2Se_{1-x}I_xS_2$ (x = 0–1.3%). The negative data over the entire temperature range suggested that Bi_2SeS_2 is an n-type semiconductor. Overall, the S for all doped samples improved with a temperature increase. The pristine Bi_2SeS_2 sample shows a relatively high S ~350 μVK^{-1} at room temperature. After iodine doping, the value dropped due to the enhanced carrier concentration. It gradually dropped to 148 μVK^{-1} as the doping level increased to 1.3%. According to the Mott formula [34], S can be expressed by the following equation:

$$S = \frac{8\pi k_B^2 T}{3eh^2} m^* \left(\frac{\pi}{3n}\right)^{\frac{2}{3}} \quad (3)$$

where k_B, h, e, m^* and n are the Boltzmann constant, the Planck constant, the electronic charge, the electron effective mass at the Fermi level, and the carrier concentration, respectively. This means increasing n would decrease S. In addition, an increase of m^* should increase the S. To present a quantitative understanding of the microscopic carrier variations, densities of state effective mass m^* are derived. Assuming that electron conduction occurs within a single parabolic band (SPB) with scattering dominated by the acoustic phonon model, the change of S with n can be plotted using the equations described elsewhere [33,35–37]. Herein, the relationship between S with the n is called the Pisarenko relation [33]. The solid curve of the SPB model fitted for the $S(n)$ function is shown in Figure 4b. The Pisarenko relationship fitted well with an m^* of $1.7m^o$, where m^o is the electron mass, and indicates the band structure was not changed by I substitution. Herein, the m^* of Bi_2SeS_2 was larger than Bi_2S_3 (~$1.5m^o$) [38], which seems the key factor leading to the higher S but lower μ of Bi_2SeS_2.

Figure 3c gives the power factor (PF). Since the enhanced σ for the doped samples completely compensated for the S decline, the resultant PF enhanced significantly. A maximum PF of 697 $\mu Wm^{-1}K^{-2}$ was achieved for $Bi_2Se_{1-x}I_xS_2$ (x = 1.1%) at 300 K, three times higher than the undoped sample, and larger than other reported data of Bi_2SeS_2 + CuI (<500 $\mu Wm^{-1}K^{-2}$ at 300 K), Bi_2S_3 (<100 $\mu Wm^{-1}K^{-2}$ at 300 K) and Bi_2Se_3 (<200 $\mu Wm^{-1}K^{-2}$ at 300 K) [19,20,39].

Figure 5a shows the total thermal conductivity (κ) for $Bi_2Se_{1-x}I_xS_2$ (x = 0–1.3%). The pristine Bi_2SeS_2 shows a low κ of 0.88 $Wm^{-1}K^{-1}$ at 300 K, which decreased further to 0.60 $Wm^{-1}K^{-1}$ at 773 K. This intrinsically low κ of Bi_2SeS_2 was due to its layered structure with weak bonding strength, because it acts as a boundary for effective phonon scattering sources in the Bi_2SeS_2 matrix [40]. The κ of the doped samples $Bi_2Se_{1-x}I_xS_2$ with x = 0.1%,

0.3%, 0.5%, 0.7%, 0.9% and 1.1% were all lower compared to the undoped sample. The lowest κ values of 0.83 $Wm^{-1}K^{-1}$ at room temperature and 0.52 $Wm^{-1}K^{-1}$ at 773 K were obtained for $Bi_2Se_{1-x}I_xS_2$ (x = 0.7%). Due to the high electronic thermal conductivity (κ_e), discussed below, the κ of $Bi_2Se_{1-x}I_xS_2$ (x = 1.3%) was slightly higher than the undoped sample.

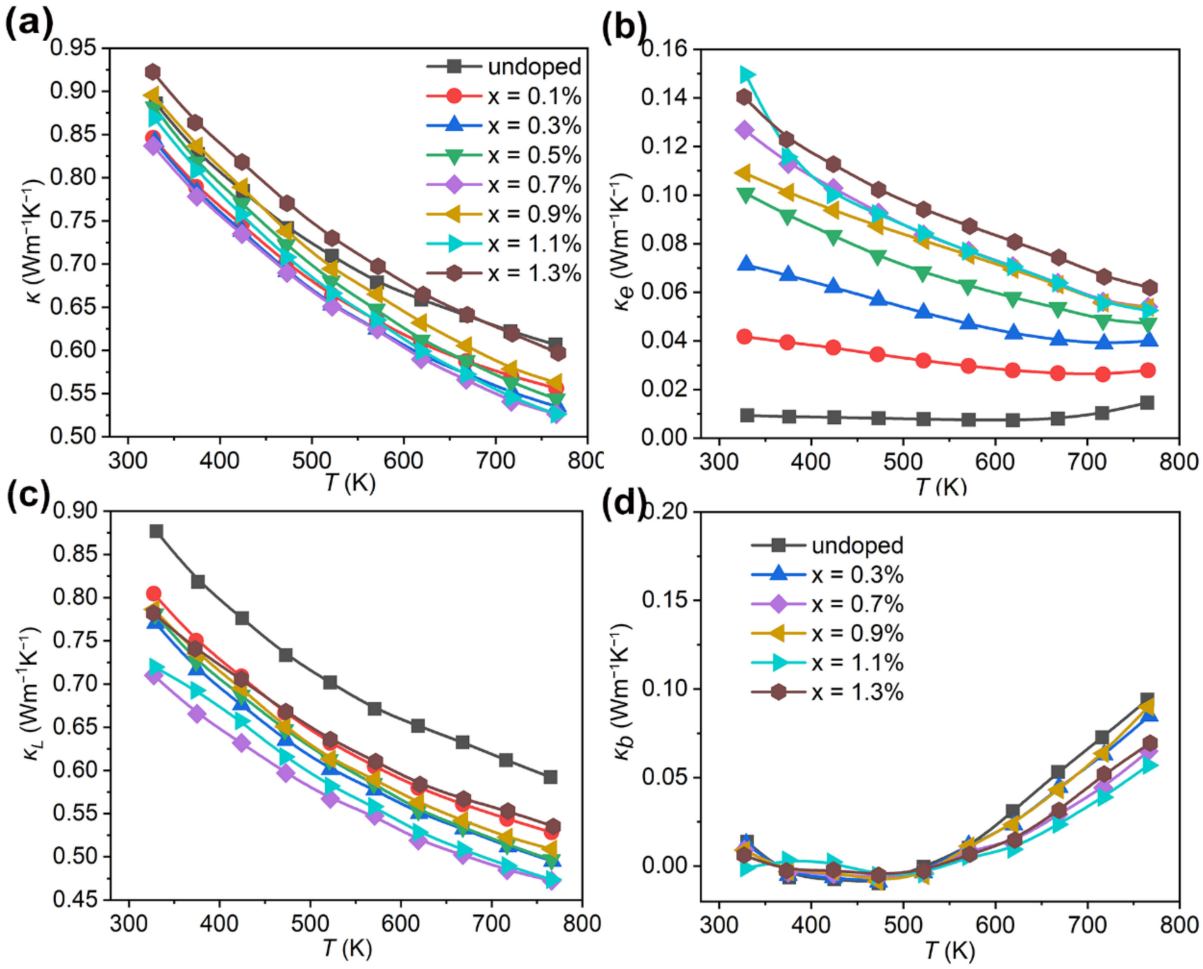

Figure 5. Thermal transport properties for $Bi_2Se_{1-x}I_xS_2$ (x = 0–1.3%). (**a**) Total thermal conductivity (κ), (**b**) electronic thermal conductivity (κ_e), (**c**) lattice thermal conductivity (κ_L), (**d**) bipolar thermal conductivity (κ_b).

Generally, the κ is the sum of the lattice thermal conductivity (κ_L) and the electronic thermal conductivity (κ_e), depicted below:

$$\kappa = \kappa_e + \kappa_L \quad (4)$$

The κ_e was obtained through the Wiedemann–Franz relationship, $\kappa_e = L\sigma T$, where σ, T, and L are the electrical conductivity, temperature, and the Lorenz number, respectively. Here, the L ranges from 1.50×10^{-8} to 1.80×10^{-8} ΩWK^{-2}, which is calculated by applying the reduced Fermi energy η. The κ_e for $Bi_2Se_{1-x}I_xS_2$ (x = 0–1.3%) is presented in Figure 5b. After doping with I, the κ_e increased due to the increased σ. It gradually improved with higher dopant levels. However, the κ_e holds only 5~17% of the κ for all doped samples, indicating that the κ is not predominated by κ_e. The temperature dependence of κ_L is shown in Figure 5c. κ_L decreased significantly over the entire temperature range after doping. At room temperature, this parameter dropped from 0.87 $Wm^{-1}K^{-1}$ for the pristine sample to 0.78 $Wm^{-1}K^{-1}$ for $Bi_2Se_{1-x}I_xS_2$ (x = 0.3%), to 0.77 $Wm^{-1}K^{-1}$ for $Bi_2Se_{1-x}I_xS_2$ (x = 0.5%),

and further to 0.71 $Wm^{-1}K^{-1}$ for $Bi_2Se_{1-x}I_xS_2$ (x = 0.7%). The significant κ_L reduction should result from the enhanced phonon scattering from the secondary phase of BiSe and the heavier relative atomic mass of I because it introduces strong phonon scattering due to the mass fluctuations. In addition, the increased grain boundary concentration caused by the reduced grain size after doping (Figure 2) also played an important role in phonon scattering. Further increasing the dopant to 0.9%, 1.1% and 1.3%, the κ_L increased slightly compared with other doped samples. One possible reason may be due to the redundancy of Bi-rich nano-precipitates with a relatively higher κ_L in the sample. Another possible reason may be the reduced grain boundary scattering due to the reduced grain boundary concentration and the increased grain size for high-doped samples. As shown in Figure 2, the grain size for the undoped sample decreased with iodine doping. However, with upping the dopant level to 0.9%, the grain size increased. The Bi-rich nano-precipitates might act as a sintering aid, contributing to the sample grain growth [41]. As for the data dependence of the temperature, the κ_L for all samples decreased with increasing temperature. However, above 600 K, the value decreases slowly. This should be attributed to the bipolar effect. In fact, for a wide-gap semiconductor at elevated temperatures or narrow-gap semiconductor at room temperature, both holes and electrons contribute to transport. This indicates that bipolar thermal conductivity (κ_b) should be considered. The κ_b was separated from κ to clarify the contribution of κ_b at high temperatures, according to the method reported by Kitagawa et al. [42]. Figure 5d shows the κ_b for some representative samples. It shows that κ_b has been reduced for the doped samples. It dropped from 0.094 $Wm^{-1}K^{-1}$ to 0.056 $Wm^{-1}K^{-1}$ for doped levels from x = 0 to x = 1.1% at 773 K, likely due to the trapping of minority carriers within the dense nanoscale regions [28]. Thus, although κ_e increased due to n optimization, the total thermal conductivity dropped by reducing κ_L and suppressing κ_b. These results indicated iodine dopants synergistically regulated the electrical and thermal transport properties of Bi_2SeS_2.

Figure 6 shows the ZT values for $Bi_2Se_{1-x}I_xS_2$ (x = 0–1.3%). Combining with the optimized power factor and reduced thermal conductivity, a maximum ZT value of 0.56 at 773 K was obtained for $Bi_2Se_{1-x}I_xS_2$ (x = 1.1%), nearly three times higher than undoped Bi_2SeS_2, and indicating that iodine is an effective n-type dopant for Bi_2SeS_2. However, compared with Br doped samples [28], the present ZT value was much lower due to the degraded power factor at high temperatures. Further efforts can be devoted to the enhancement of the electrical transport properties of Bi_2SeS_2 at high temperature, such as dual-doping.

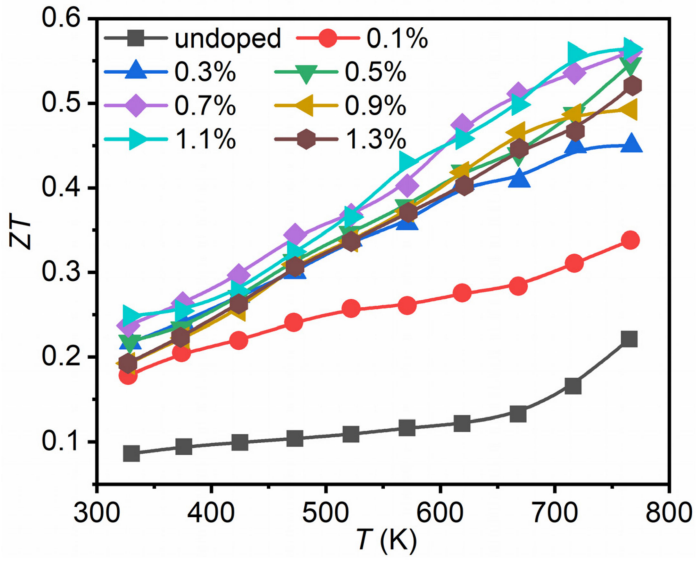

Figure 6. Dimensionless figure of merit (ZT) for $Bi_2Se_{1-x}I_xS_2$ (x = 0–1.3%).

4. Conclusions

A series of $Bi_2Se_{1-x}I_xS_2$ (x = 0–1.3%) samples were prepared by combining a solid state reaction with SPS. Those results revealed that iodine is an effective n-type dopant for Bi_2SeS_2. The electrical conductivity increased due to optimized carrier concentration produced by the carrier provided defect I_{se}. Combined with a moderate Seebeck coefficient (>150 μVK^{-1}) due to its large effective mass, a high power factor of 697 $\mu Wm^{-1}K^{-2}$ at 300 K was obtained. In addition, the total thermal conductivity decreased, primarily due to the decreased lattice thermal conductivity resulting from the enhanced phonon scattering. Thus, a maximum *ZT* of 0.56 at 773 K was achieved for $Bi_2Se_{1-x}I_xS_2$ (x = 1.1%), nearly three times higher than the pristine sample.

Author Contributions: Conceptualization, F.L.; methodology, C.L. (Chongbin Liang) and B.J.; validation, F.L. and Y.C.; formal analysis, C.L. (Chongbin Liang) and C.L. (Chen Liu); investigation, C.L. (Chongbin Liang) and B.J.; data curation, C.L. (Chongbin Liang) and Z.Z.; writing—original draft preparation, C.L. (Chongbin Liang); writing—review and editing, B.J. and F.L.; supervision, P.F. All authors have read and agreed to the published version of the manuscript.

Funding: This work was supported by the National Natural Science Foundation of China (No. 52072248), Natural Science Foundation of Guangdong Province of China (No. 2021A1515012128, No. 2018A030313574) and Natural Science Foundation of SZU (No. 827-000357).

Institutional Review Board Statement: Not applicable.

Informed Consent Statement: Not applicable.

Data Availability Statement: The data presented in this study are available on request from the corresponding author.

Conflicts of Interest: The authors declare no conflict of interest.

References

1. Bérardan, D.; Guilmeau, E.; Maignan, A.; Raveau, B. In_2O_3: Ge, a promising n-type thermoelectric oxide composite. *Solid State Commun.* **2008**, *146*, 97–101. [CrossRef]
2. Chen, G.; Dresselhaus, M.S.; Dresselhaus, G.; Fleurial, J.P.; Cailla, T. Recent developments in thermoelectric materials. *Int. Mater. Rev.* **2003**, *48*, 45–66. [CrossRef]
3. Bell, L.E. Cooling, heating, generating power, and recovering waste heat with thermoelectric systems. *Science* **2008**, *321*, 1457–1461. [CrossRef] [PubMed]
4. DiSalvo, F.J. Thermoelectric cooling and power generation. *Science* **1999**, *285*, 703–706. [CrossRef]
5. Rowe, D.M. *CRC Handbook of Thermoelectrics*; CRC Press: Boca Raton, FL, USA, 1995.
6. Nolas, G.S. *Basic Principles and New Materials Developments*; Springer: New York, NY, USA, 2001.
7. Zhang, X.; Zhao, L.D. Thermoelectric materials: Energy conversion between heat and electricity. *J. Mater.* **2015**, *1*, 92–105. [CrossRef]
8. Yang, L.; Chen, Z.G.; Dargusch, M.S.; Zou, J. High performance thermoelectric materials: Progress and their applications. *Adv. Energy Mater.* **2018**, *8*, 6. [CrossRef]
9. Slack, G. *New Materials and Performance Limits for Thermoelectric Cooling*; CRC: Boca Raton, FL, USA, 1995.
10. Pei, Y.; Shi, X.; LaLonde, A.; Wang, H.; Chen, L.; Snyder, G.J. Convergence of electronic bands for high performance bulk thermoelectric. *Nature* **2011**, *473*, 66–69. [CrossRef]
11. Heremans, J.P.; Thrush, C.M.; Morelli, D.T. Thermopower enhancement in lead telluride nanostructures. *Phys. Rev. B* **2004**, *70*, 11–15. [CrossRef]
12. Liu, H.L.; Yuan, X.; Lu, P.; Shi, X.; Xu, F.F.; He, Y.; Tang, Y.S.; Bai, S.Q.; Zhang, W.Q.; Chen, L.D.; et al. Ultrahigh thermoelectric performance by electron and phonon critical scattering in $Cu_2Se_{1-x}I_x$. *Adv. Mater.* **2013**, *25*, 6607–6612. [CrossRef]
13. Biswas, K.; He, J.; Blum, I.D.; Wu, C.I.; Hogan, T.P.; Seidman, D.N.; Dravid, V.P.; Kanatzidis, M.G. High-performance bulk thermoelectrics with all-scale hierarchical architectures. *Nature* **2012**, *489*, 414–418. [CrossRef]
14. Liu, W.S.; Zhang, Q.; Lan, Y.; Chen, S.; Yan, X.; Zhang, Q.; Wang, H.; Wang, D.; Chen, G.; Ren, Z. Thermoelectric property studies on Cu-doped n-type $Cu_xBi_2Te_{2.7}Se_{0.3}$ nanocomposites. *Adv. Energy Mater.* **2011**, *1*, 577–587. [CrossRef]
15. Finefrock, S.W.; Yang, H.; Fang, H.; Wu, Y. Thermoelectric properties of solution synthesized nanostructured materials. *Annu. Rev. Chem. Biomol. Eng.* **2015**, *6*, 247–266. [CrossRef]
16. Hu, L.P.; Zhu, T.J.; Wang, Y.G.; Xie, H.H.; Xu, Z.J.; Zhao, X.B. Shifting up the optimum figure of merit of p-type bismuth telluride-based thermoelectric materials for power generation by suppressing intrinsic conduction. *NPG Asia Mater.* **2014**, *6*, e88. [CrossRef]

17. Ge, Z.H.; Zhao, L.D.; Wu, D.; Liu, X.Y.; Zhang, B.P.; Li, J.F.; He, J.Q. Low-cost, abundant binary sulfides as promising thermoelectric materials. *Mater. Today* **2016**, *19*, 227–239. [CrossRef]
18. Farooq, M.U.; Butt, S.; Gao, K.W.; Sun, X.G.; Pang, X.L.; Khan, S.U.; Xu, W.; Mohmed, F.; Mahmood, A.; Mahmood, N. Enhanced thermoelectric efficiency of $Cu_{2-x}Se$-Cu_2S composite by incorporating Cu_2S nanoparticles. *Ceram. Int.* **2016**, *42*, 8395–8401. [CrossRef]
19. Liu, W.S.; Lukas, K.C.; McEnaney, K.; Lee, S.; Zhang, Q.; Opeil, C.P.; Chen, G.; Ren, Z.F. Studies on the Bi_2Te_3-Bi_2Se_3-Bi_2S_3 system for mid-temperature thermoelectric energy conversion. *Energy Environ. Sci.* **2013**, *6*, 552–560. [CrossRef]
20. Ge, Z.H.; Qin, P.; He, D.S.; Chong, X.Y.; Feng, D.; Ji, Y.H.; Feng, J.; He, J.Q. Highly enhanced thermoelectric properties of Bi/Bi_2S_3nanocomposites. *ACS Appl. Mater. Inter.* **2017**, *9*, 4828–4834. [CrossRef]
21. Biswas, K.; Zhao, L.D.; Kanatzidis, M.G. Tellurium-free thermoelectric: The anisotropic n-type semiconductor Bi_2S_3. *Adv. Energy Mater.* **2012**, *2*, 634–638. [CrossRef]
22. Ge, Z.H.; Zhang, B.P.; Shang, P.P.; Li, J.F. Control of anisotropic electrical transport property of Bi_2S_3 thermoelectric polycrystals. *J. Mater. Chem.* **2011**, *21*, 9194–9200. [CrossRef]
23. Chen, Y.; Wang, D.Y.; Zhou, Y.L.; Pang, Q.T.; Shao, J.W.; Wang, G.T.; Wang, J.F.; Zhao, L.D. Enhancing the thermoelectric performance of Bi_2S_3: A promising earth abundant thermoelectric material. *Front. Phys.* **2019**, *14*, 13601. [CrossRef]
24. Kawamoto, Y.; Iwasaki, H. Thermoelectric properties of $(Bi_{1-x}Sb_x)_2S_3$ with orthorhombic structure. *J. Electron. Mater.* **2014**, *43*, 1475. [CrossRef]
25. Zhao, L.D.; Zhang, B.P.; Liu, W.S.; Zhang, H.L.; Li, J.F. Enhanced thermoelectric properties of bismuth sulfide polycrystals prepared by mechanical alloying and spark plasma sintering. *J. Solid State Chem.* **2008**, *181*, 3278–3282. [CrossRef]
26. Ge, Z.H.; Zhang, B.P.; Li, J.F. Microstructure composite-like Bi_2S_3 polycrystals with enhanced thermoelectric properties. *J. Mater. Chem.* **2012**, *22*, 17589–17594. [CrossRef]
27. Li, F.; Ruan, M.; Jabar, B.; Liang, C.B.; Chen, Y.X.; Ao, D.W.; Zheng, Z.H.; Fan, P.; Liu, W.S. High thermoelectric properties achieved in environmentally friendly sulfide compound Bi_2SeS_2 by nanoenginnering. *Nano Energy* **2021**, *88*, 106273. [CrossRef]
28. Jabar, B.; Li, F.; Zheng, Z.H.; Mansoor, A.; Zhu, Y.B.; Liang, C.B.; Ao, D.W.; Chen, Y.X.; Liang, G.X.; Fan, P.; et al. Homo-composition and hetero-structure nanocomposite *Pnma* Bi_2SeS_2–*Pnnm* Bi_2SeS_2 with high thermoelectric performance. *Nat. Commun.* **2021**, *12*, 7192. [CrossRef]
29. Li, L.; Liu, Y.; Dai, J.Y.; Zhu, H.X.; Hong, A.J.; Zhou, X.H. Thermoelectric property studies on $Cu_xBi_2SeS_2$ with nano-scale precipitates Bi_2S_3. *Nano Energy* **2015**, *12*, 447–456. [CrossRef]
30. Ruan, M.; Li, F.; Chen, Y.X.; Zheng, Z.H.; Fan, P. Te-free compound Bi_2SeS_2 as a promising mid-temperature thermoelectric material. *J. Alloys Compd.* **2020**, *849*, 156677. [CrossRef]
31. Liu, Z.; Pei, Y.; Geng, H.; Zhuo, J.; Meng, X.; Cai, W.; Liu, W.; Sui, J. Enhanced thermoelectric properties of Bi_2S_3 by synergistically action of bromine substitution and copper nanoparticles. *Nano Energy* **2015**, *13*, 554–562. [CrossRef]
32. Ji, W.; Shi, X.L.; Liu, W.; Yuan, H.; Zheng, K.; Wan, B.; Shen, W.; Zhang, Z.; Fang, C.; Wang, Q.; et al. Boosting the thermoelectric performance of n-type Bi_2S_3 by hierarchical structure manipulation and carrier density optimization. *Nano Energy* **2021**, *87*, 106171. [CrossRef]
33. Wei, T.R.; Wang, H.; Gibbs, Z.M.; Wu, C.F.; Snyder, G.J.; Li, J.F. Thermoelectric properties of Sn-doped p-type Cu_3SbSe_4: A compound with large effective mass and small band gap. *J. Mater. Chem. A* **2014**, *2*, 13527–13533. [CrossRef]
34. Snyder, G.J.; Toberer, E.S. Complex thermoelectric materials. *Nat. Mater.* **2008**, *7*, 105–114. [CrossRef] [PubMed]
35. Pichanusakorn, P.; Bandaru, P.R. Minimum length scales for enhancement of the power factor in thermoelectric nanostructures. *J. Appl. Phys.* **2010**, *107*, 0743047. [CrossRef]
36. Pichanusakorn, P.; Bandaru, P.R. The optimal Seebeck coefficient for obtaining the maximum power factor in thermoelectrics. *Appl. Phys. Lett.* **2009**, *94*, 22310822. [CrossRef]
37. May, A.F.; Toberer, E.S.; Saramat, A.; Jeffrey Snyder, G. Characterization and analysis of thermoelectric transport in n-type $Ba_8Ga_{16-x}Ge_{30+x}$. *Phys. Rev. B Condens. Matter Mater. Phys.* **2009**, *80*, 125205. [CrossRef]
38. Guo, J.; Zhang, Y.X.; Wang, Z.Y.; Zheng, F.; Ge, Z.H.; Fu, J.; Fen, J. High thermoelectric properties realized in earth-abundant Bi_2S_3 bulk via carrier modulation and multi-nano-precipitates synergy. *Nano Energy* **2020**, *78*, 105227. [CrossRef]
39. Hor, Y.S.; Richardella, A.; Roushan, P.; Xia, Y.; Checkelsky, J.G.; Yazdani, A.; Hasan, M.Z.; Ong, N.P.; Cava, R.J. P-type Bi_2Se_3 for topological insulator and low temperature thermoelectric applications. *Phys. Rev. B* **2009**, *79*, 195208. [CrossRef]
40. Yang, L.; Chen, Z.G.; Hong, M.; Han, G.; Zou, J. Enhanced thermoelectric performance of nanostructured Bi_2Te_3 through significant phonon scattering. *ACS Appl. Mater. Inter.* **2015**, *7*, 23694–23699. [CrossRef]
41. Zheng, Z.H.; Wang, T.; Jabar, B.; Ao, D.W.; Li, F.; Chen, Y.X.; Liang, G.X.; Luo, J.T.; Fan, P. Enhanced thermoelectric performance in n-type Bi_2O_2Se by an exquisite grain boundary engineering approach. *ACS Appl. Energy Mater.* **2021**, *4*, 10290–10297. [CrossRef]
42. Kitagawa, H.; Wakatsuki, M.; Nagaoka, H.; Noguchi, H.; Isoda, Y.; Hasezaki, K.; Noda, Y. Temperature dependence of thermoelectric properties of Ni-doped $CoSb_3$. *J. Phys. Chem. Solids* **2005**, *66*, 1635–1639. [CrossRef]